Pulsed laser-plasma gamma radiation source for radiography

V.A. Flegentov, K.V. Safronov, S.A. Gorokhov,
A.S. Tishchenko, S.F. Kovaleva, A.V. Potapov, A.V. Pavlenko

Abstract. **We have performed experiments on the generation of relativistic electron beams in helium gas jets (electron density $\sim 10^{20}$ cm^{-3}) using a femtosecond Ti:sapphire laser. Electron beams with a total charge of 0.2–0.5 nC, a maximum electron energy of up to 60 MeV, and a divergence of up to 300 mrad are recorded. The generated electron beams are converted into bremsstrahlung X-rays using a Ta plate 2 mm thick. The average dose of bremsstrahlung radiation in the air at a distance of 1 m from the source was 5.4 ±1.7 mrad per pulse. The emitting region size measured by the blurriness of the X-ray image is about 650 µm (FWHM).**

1. Introduction

Laser-plasma electron beam accelerators are attractive sources of bremsstrahlung X-rays (BXRs) with unique characteristics: high quantum energy (tens of MeV), short pulse duration (units of ps), and small size of the emitting region (hundreds of microns) [1, 2]. The disadvantage that prevents the widespread practical application of such sources in pulsed radiography is the small number of accelerated electrons.

Recently, significant progress has been made in laser-plasma generation of electron beams in low-density gas targets ($n_e \sim 10^{18}$ cm^{-3}); however, the total charge of the beams accelerated in such targets does not exceed several tens of pC [3, 4]. One of the ways to increase the number of electrons accelerated in a laser plasma is to increase its density [5, 6].

In this work, we experimentally investigate the generation of accelerated electron beams during the interaction of high-intensity ultrashort laser pulses with high-density gas targets (up to 2×10^{20} cm^{-3}). The characteristics of the generated electron beams (energy spectrum, total charge, and angular divergence) are studied under various conditions of gas target irradiation (jet density and focusing sharpness).

The generated electron beams were converted into BXR flashes using a tantalum converter. The X-ray source param-

V.A. Flegentov, K.V. Safronov, S.A. Gorokhov, A.S. Tishchenko, S.F. Kovaleva, A.V. Potapov, A.V. Pavlenko Russian Federal Nuclear Center – Zababakhin All-Russia Research Institute of Technical Physics (RFNC-VNIITF), ul. Vasil'eva 13, 456770 Snezhinsk, Chelyabinsk region, Russia; e-mail: vflegentov@gmail.com

eters that are important for applications in the field of radiography are determined: the source yield, its spectrum, and the emitting region size.

2. Experimental

Experiments on the generation of relativistic electron beams from dense gas jets were carried out using a femtosecond Ti:sapphire laser with a centre laser wavelength $\lambda_{las} = 800$ nm, pulse duration $\tau_{las} = 25$ fs, and energy E_{las} up to 2.5 J. A linearly polarised laser beam with an aperture of 80 mm was focused by an off-axis parabolic mirror with a relative aperture of 1:10. The beam diameter $2r_0$ in the focal plane was 14.8 µm (FWHM), and 50% of the incoming energy was concentrated inside this region. The laser radiation intensity during the experiments was $(1–3) \times 10^{19}$ W cm^{-2}.

As a target in our experiments, we used He jets emitted by an aluminium conical nozzle with an outlet channel of ∅1 mm and a critical diameter of 0.45 mm [7]. The laser beam was focused onto the gas target using an auxiliary solid-state target, which, when adjusted, was brought to the front geometric edge of the nozzle outlet. The pulsed gas supply to the nozzle channel was performed using a high-speed Parker Hannifin gas valve as part of the target assembly. The gas density in the jet was determined by the pressure in the gas supply system, which was regulated in the range of 10–60 atm.

The spatial distribution of molecular density in gas jets was measured in a vacuum chamber using a pulsed Mach–Zehnder interferometer [8]. A laser source with $\lambda = 532$ nm and $\tau = 7$ ns was used in the measurements. To simplify the measurements, we used Ar as a working gas, the refractive index of which is several times higher than that of He. Since Ar and He are monoatomic gases with the same adiabatic exponent ($\gamma = 5/3$), the molecular density profiles in the jet will be similar when these gases are used. The spatial distribution of the refractive index was reconstructed using the Abel convolution [9] under the assumption of axial symmetry of the gas jet. Figure 1a shows an example of the reconstructed electron density distribution in a jet for He at a pressure of 45 atm (recalculated according to Ar data). The corresponding density profiles of the gas jet, measured at various heights z from the nozzle cutoff, are shown in Fig. 1 b. It can be seen that the density profile at $z = 1$ mm (the height of the laser beam focusing in the experiments) is dome-shaped with a front of ~ 530 µm (at a level from 0.1 to 0.9). According to the results of measurements, the electron density on the gas jet axis in the experiments could vary in the range $(0.4–2.2) \times 10^{20}$ cm^{-3}.

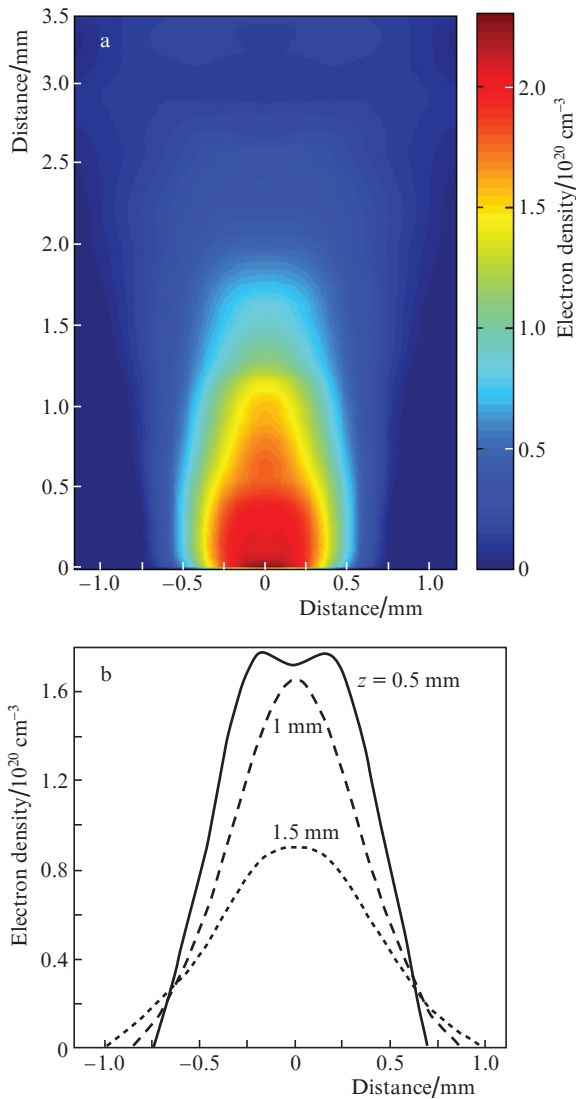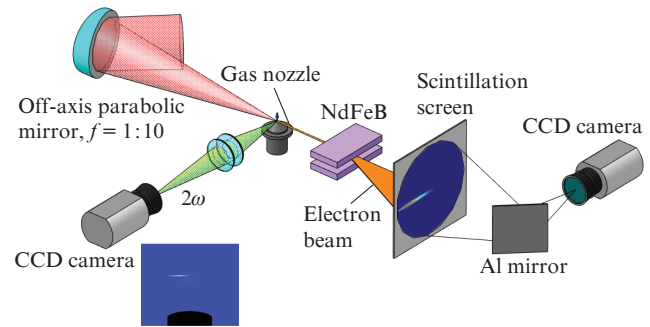The scheme of experiments on measuring the parameters of electron beams generated by the interaction of ultrashort

Figure 1. (Colour online) (a) Spatial distribution of electron density in the gas jet and (b) electron density profiles at various heights z from the nozzle cutoff (He, 45 atm).

Figure 2. Scheme of experiments on laser-plasma acceleration of electrons.

laser pulses with gas jets is shown in Fig. 2. The energy distribution of accelerated electrons was measured using a scintillation spectrometer with plane-parallel magnets (NdFeB). The spectrometer of electrons was placed at a distance of 72 mm from the gas target along the laser beam propagation axis. The magnetic field in the gap between the magnets was 0.77 ± 0.04 T. An electron beam deflected in the magnetic field was directed onto a thin $Gd_2O_2S:Tb$ (Kodak Lanex Regular) scintillation screen. To protect the screen from the effect of laser radiation passing in the forward direction, a Ti foil with a thickness of 50 μm was installed in front of the screen. Due to the small thickness of the scintillation screen, its sensitivity to electrons with energies from 1 to 100 MeV is almost constant [10, 11]. The scintillation screen glow caused by accelerated electrons was recorded by a 16-bit CCD camera with a lens mounted in front of the camera. In the recording channel, optical filters SZS-21 and OS-11 [12] were used, separating out radiation with a spectrum in the vicinity of 546 nm. To reduce the noise when recording images on the scintillation screen, the CCD camera was removed from the zone of direct

exposure to a beam of relativistic electrons using a rotary Al mirror. The spectrometer design made it possible to record electrons with an energy of 12 MeV and higher. The spectrometer energy resolution was ~3 % for electron energies of 20 MeV and ~24 % for energies of 100 MeV.

The angular divergence and total charge of the accelerated electron beams were measured from images obtained on the same scintillation screen in the absence of a magnetic field. The screen was located at a distance of 210 mm from the gas target; a 300-μm-thick Pb filter was installed in front of the screen, which cut off low-energy electrons with energies of up to several MeV [13] and served as a shield against direct incidence of laser radiation onto the screen. The screen glow was recorded using the optical path of a magnetic electron spectrometer.

In addition, in the experiments, the glow of the interaction region of laser radiation with a gas jet was recorded. The images were recorded using a side-mounted 8-bit CCD camera (Fig. 2) in the spectral range of 0.38–0.42 μm, which was provided by the installation of SZS-21 and FS-7 light filters.

When BXRs were generated by accelerated electron beams, a flat Ta converter with a thickness of 2 mm was used in experiments (Fig. 3). The converter was placed behind the gas target at a distance of 2 mm from it. The generated bremsstrahlung radiation was released from the vacuum target chamber through an Al-flange with a thickness of 16 mm. The energy fluence of X-ray radiation emitted in the forward direction (in a cone with an angular opening of ±2.5°) without taking into account the re-scattered X-rays was measured with an SSDI-40 pulsed-current scintillation detector. The detector's sensitive volume (a ∅63 × 63 mm polystyrene cylinder) was located outside the vacuum chamber at a distance of 400 cm from the tantalum converter.

To measure the transverse size of the BXR emitting region in experiments, a 200-mm-thick tungsten block was installed behind the Ta converter, one of the side surfaces of which had a curvature radius of 500 mm and was oriented tangentially to the laser beam axis (see Fig. 3). The block was an opaque barrier for BXR quanta with energies up to several tens of MeV and was used to form a contrast difference in its intensity at the detector. Shadow X-ray images were recorded on photostimulated storage phosphor screens (BAS-MS imaging plates, Fuji), which were installed outside the target chamber at a distance of 150 cm from the converter. The transverse size of the emitting region was determined by the blurring of the shadow edge in the image.
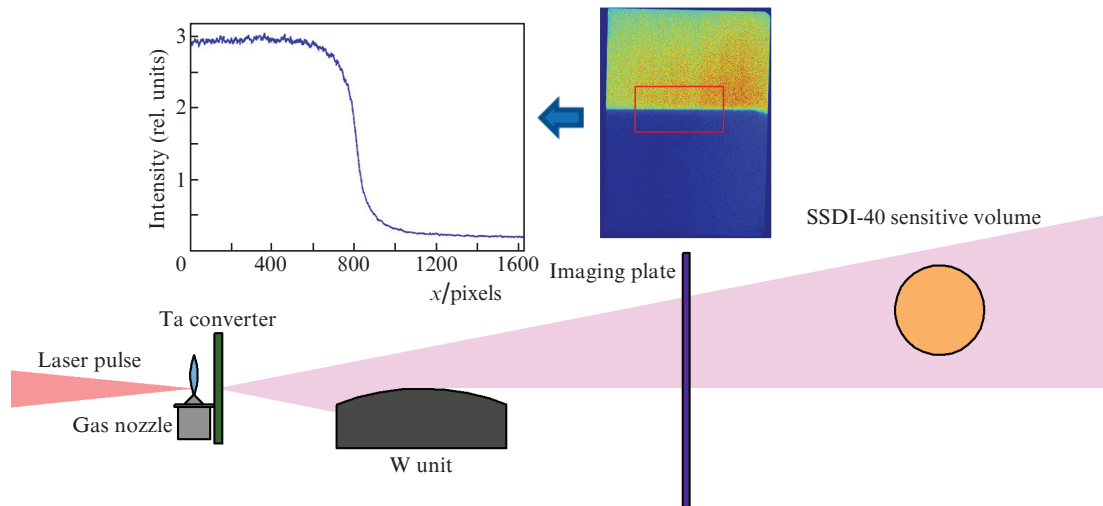
Figure 3. Scheme of experiments on generation of BXRs.

3. Experimental results

3.1. Measurement of characteristics of accelerated electron beams

Figures 4 and 5 show the imprints of the generated electron beams on the scintillation screen, recorded in the absence of a magnetic field. At a gas pressure in the nozzle system up to 10 atm ($n_e \sim 4 \times 10^{19}$ cm^{-3}), bright spots from collimated beams with a divergence of $\sim$10 mrad are observed against the background of a glow caused by a shapeless beam of
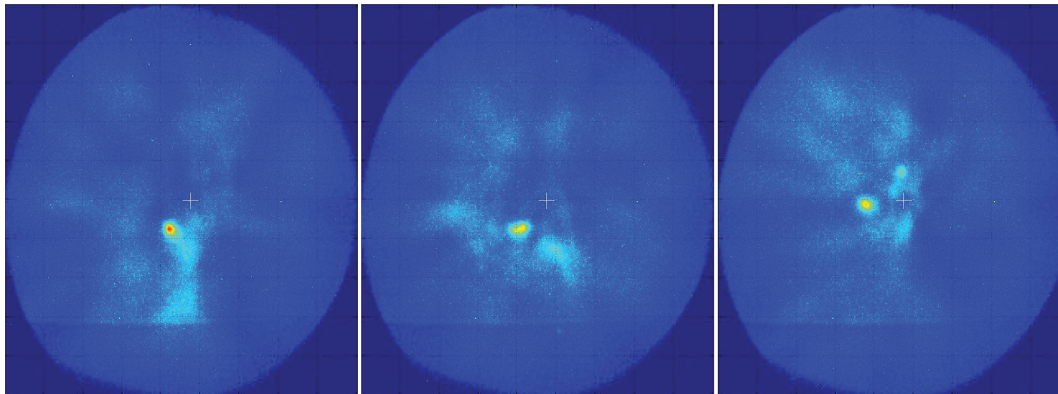

Figure 4. (Colour online) Imprints of electron beams on the scintillation screen in three subsequent pulses at a helium pressure of 10 atm in the gas nozzle system.

Figure 5. (Colour online) Imprints of electron beams on the scintillation screen in three subsequent pulses at a helium pressure of 60 atm in the gas nozzle system. A grid with an angular step of 100 mrad is applied to the images.
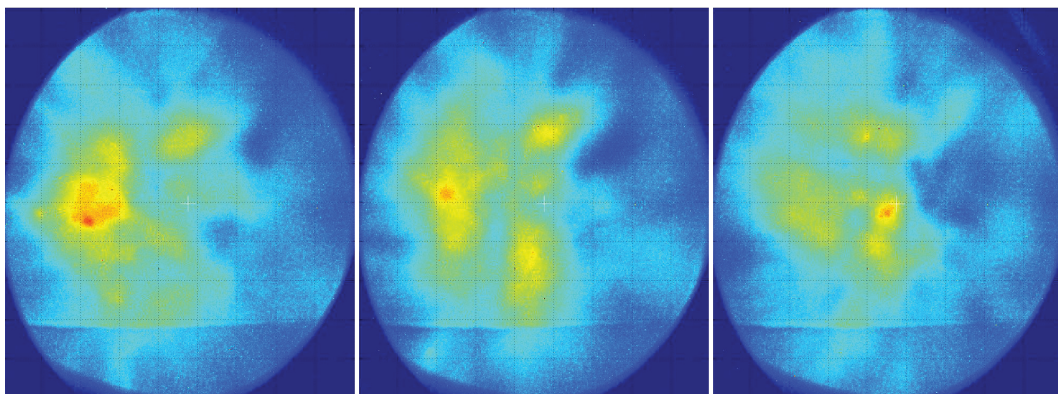
greater divergence (Fig. 4). The angular instability of the collimated part of the beam reached 30 mrad from pulse to pulse.

As the gas pressure in the nozzle system increases to 60 atm ($n_e \sim 2.2 \times 10^{20}$ cm^{-3}), the glow brightness of the scintillation screen increases (Fig. 5). The brightness distribution of the electron beam on the screen has an inhomogeneous structure; no separate collimated beams are observed. The angular size of the beam's bright part, which contains more than 50% of glow energy, reaches $\sim$300 mrad.

An example of images of the glow of plasma channels in the region of laser radiation interaction with a helium jet in the gas supply system at pressures of 10 and 60 atm is shown in Fig. 6. At high pressures, filamentation with the formation of multiple plasma channels is observed. The bright, inhomogeneous glow along the channel is interrupted before reaching the gas jet axis. At low pressures, filamentation is not observed. The maximum glow brightness falls on the gas target axis. The glow images of the plasma channels are qualitatively consistent with the sizes of the imprints of electron beams on the scintillation screen: the angular opening of the beams increases during filamentation.
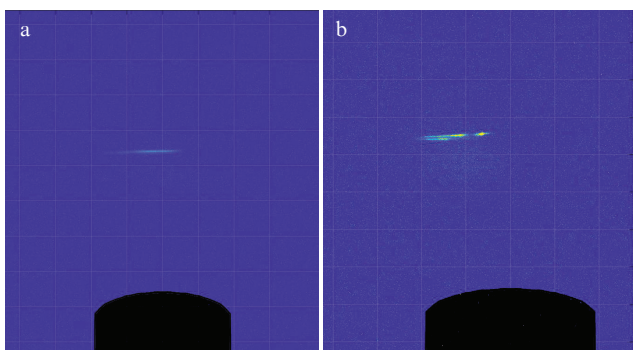

Figure 6. (Colour online) Photographs of the glow of the interaction region of a laser pulse with a gas helium target. The laser pulse propagates from left to right: (a) $p = 10$ atm, $E_{las} = 1.68$ J; (b) $p = 60$ atm, $E_{las} = 1.74$ J. A spatial grid with a step of 400 μm is superimposed on the images.

Since the sensitivity of the used scintillation screen was nearly constant for electrons with energies above 1 MeV [10], the brightness of the imprints on the scintillation screen served as a measure of the electron beam charge Q_{beam} that caused this glow:

$$Q_{beam} = \frac{\int_0^{X,Y} I(x,y)\,\mathrm{d}x\mathrm{d}y}{\xi_{monitor}}, \qquad (1)$$

where $I(x,y)$ is the beam image brightness at the point with spatial coordinates x and y; and $\xi_{monitor}$ is the sensitivity of the image recording system.

Figure 7 shows the results of measurements of the total charge of electron beams (given per unit of laser pulse energy) generated at various densities of the gas target. With an increase in the jet density, a proportional increase in the charge of the generated beams is observed. The maximum total charge of the beam measured in the experiments was 0.5 ± 0.1 nC. In this case, the displacement of the laser beam waist relative to the nominal position at a distance of up to
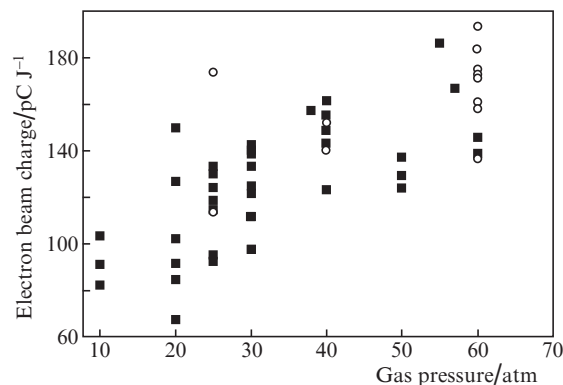
Figure 7. Results of measurements of the electron beam's total charge as a function of the gas pressure in the target assembly system. Measurements are presented at tight focusing of the laser pulse (■) and detuning by -800 μm (○).

800 μm did not lead to a significant decrease in the total charge of the beam.

Figure 8 shows the results of measurements of the spectra of electron beams generated in experiments at various gas pressures in the nozzle system. Images of electron beams deflected in a magnetic field, obtained using a magnetic scintillation spectrometer, are shown in Fig. 8a. Figure 8b shows the energy spectra of electron beams accelerated in experiments with gas jets of various densities. All recorded electron beam spectra are exponential. Electron spectra [$\mathrm{d}N_e/\mathrm{d}E \sim \exp(-E/T_e)$] with a temperature T_e from 2.7 to 7.4 MeV were observed.

With an increase in the gas pressure in the nozzle system from 10 to 60 atm, the maximum recorded electron energy monotonically decreased from 60 to 20 MeV (Fig. 8c).

It should be noted that in experiments conducted at gas pressures less than 30 atm, accelerated electron beams with energy spectra covering the high-energy region (Fig. 8a) were not recorded by a magnetic spectrometer in every pulse. Apparently, this is due to the significant instability of the beam's angular directivity in this lasing regime. On the contrary, at a high gas pressure (more than 30 atm), the images of the deflected electron beam were reliably recorded, and the energy spectra of the electron beams were characterised by good stability.

### 3.2. Measurement of BXR source characteristics

The energy flux of X-rays that has passed through the SSDI-40 sensitive volume is related to the charge Q_{det} taken from the detector as follows:

$$Q_{det} = k \int_0^{E_{max}} E_\gamma \frac{\mathrm{d}N}{\mathrm{d}E_\gamma} w(E_\gamma)\,\mathrm{d}E_\gamma = \eta(E_\gamma)\,\Phi_\gamma, \qquad (2)$$

where E_γ is the energy of quanta; $\mathrm{d}N/\mathrm{d}E_\gamma$ is the spectrum of quanta; $w(E_\gamma)$ is the absorption coefficient of radiation energy in the scintillator; k is the instrument constant; $\eta(E_\gamma) = kw(E_\gamma)$ is the detector sensitivity; and

$$\Phi_\gamma = \int_0^{E_{max}} E_\gamma \frac{\mathrm{d}N}{\mathrm{d}E_\gamma}\,\mathrm{d}E_\gamma$$

is the radiation energy fluence.
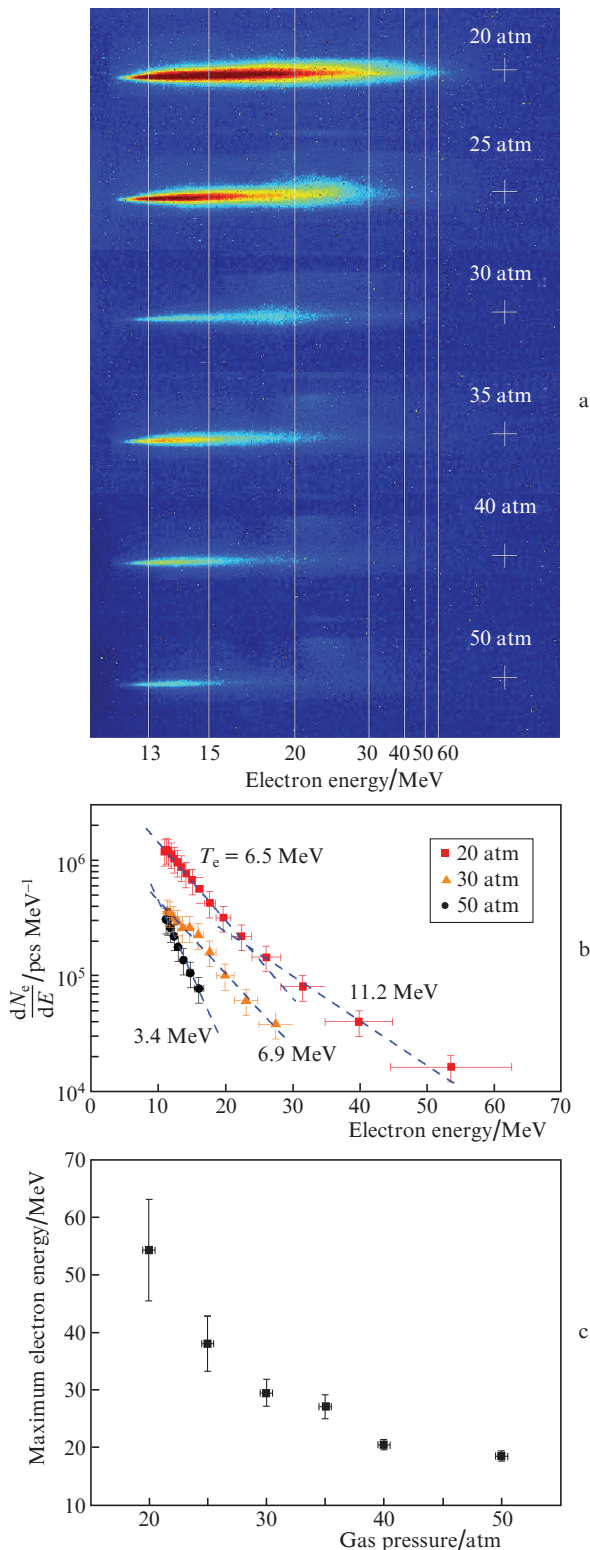
Figure 8. (Colour online) Energy spectra of electron beams at various helium pressures: (a) original images, (b) energy distributions of electron beams, and (c) dependence of the maximum recorded electron energy on the gas pressure.

The detector sensitivity η was measured using a ^{60}Co isotope source only for quanta with an energy of $E_\gamma = 1.25$ MeV. Therefore, when measuring the BXR energy fluence having a continuous spectrum, it is necessary to take into account the coefficient $w(E_\gamma)$. For the detector in use, the values of

$w(E_\gamma)$ for quanta with energies of 0.1 and 1 MeV are no more than twofold different.

The BXR yield as a function of the gas pressure in the targets assembly system is shown in Fig. 9. With an increase in the gas jet density, it grows according to a close-to-exponential law. The gas target displacement from the beam waist position by $400-800$ μm led to a significant increase in the BXR yield, especially at a low jet density. This regime was subsequently chosen as the optimal one. The statistics of measurements of the BXR yield in the specified regime in a series of more than 70 shots with fixed parameters is shown in Fig. 10. The BXR yield was $(7.1 \pm 2.5) \times 10^9$ MeV J^{-1} sr^{-1}.
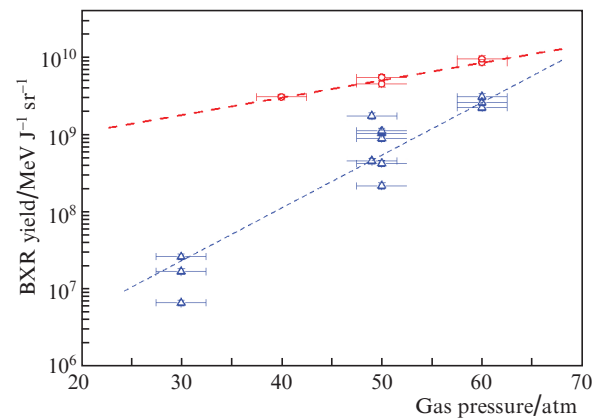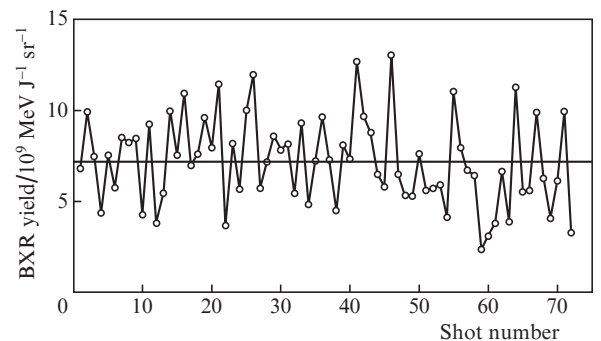

Figure 9. Specific (per unit of laser energy) BXR yield as a function of the helium pressure and focusing conditions: (△) tight focusing and (○) at a detuning of -400 μm.

Figure 10. X-ray yield in a series of experiments with fixed parameters: $E_{las} = 2.06 \pm 0.06$ J, $\tau_{las} = 27$ fs, focusing detuning -800 μm, and helium at a pressure of 60 ± 2.5 atm. The horizontal line indicates the average yield in the series, equal to $(7.1 \pm 2.5) \times 10^9$ MeV J^{-1} sr^{-1}.
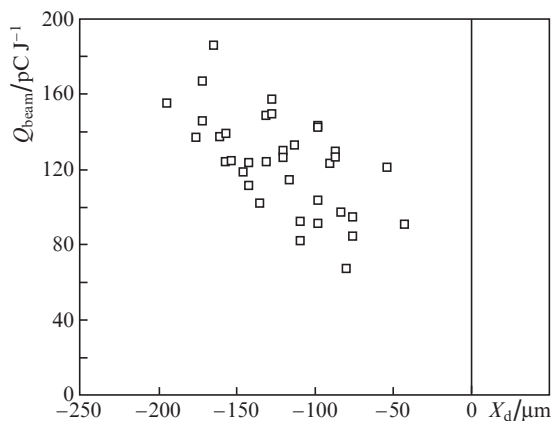
Measurements of the transverse size of the BXR emitting region were performed in a similar regime (see Fig. 3). Since the recording was carried using the photostimulated imaging plates, the measurements were only conducted in a few experiments. Images from the detectors were read out with a spatial resolution of 25 μm. The emitting region size was determined by the width of the line spread function (FWHM) obtained during image processing with allowance for the magnification factor determined by the recording geometry. Based on five experiments, the source size amounted to 650 μm.

4. Discussion of the results

The results of measurements of the characteristics of electron beams accelerated in experiments have shown that they all have energy spectra of the form $dN_e/dE_e \sim E_e \exp(-E_e/T_e)$ with an effective 'temperature' T_e. This shape of electron spectra is typical of the SM-LWFA regime [14] that occurs when exposed to a laser pulse, the duration τ_{las} of which exceeds the period $\tau_p = \sqrt{\pi m_e/n_e e^2}$ of plasma oscillations of the medium. In our experiments, the ratio τ_{las}/τ_p varied in the range 1.6–3.5 (valid only for the axial region of the jet, where τ_p is minimal). Previously, a decrease in the maximum energy of accelerated electrons was already observed with an increase in the density of electrons in the medium during acceleration in the SM-LWFA regime [15].

Note that the experimentally observed decrease in the particle energy is accompanied by an increase in their number. In this case, the laser pulse energy conversion into electrons remains virtually unchanged and, regardless of the gas density, amounts to 0.2%–0.25%. This effect can probably be explained by a secondary process: After depletion of the laser driver energy, the accelerated electrons themselves generate a plasma wave, into which, due to self-injection, new electrons are drawn from the periphery of the plasma channel. There is a transition from the laser wakefield acceleration (LWFA) regime to the so-called plasma wakefield acceleration (PWFA) regime [16]. In this case, the original electron beam loses energy to maintain the plasma wave, and this energy is partially transferred to electrons accelerated in the PWFA regime [17].

The higher the plasma density, the earlier the depletion of the laser pulse energy and the transition to the PWFA stage occur. The place where the acceleration regimes change can be determined from experimental images of the gas jet by the cutoff position of the plasma glow at the frequency of the second harmonic of laser radiation. Figure 11 shows the dependence of the beam charge on the coordinate of the glow cutoff point relative to the jet axis X_d, according to which the earlier the PWFA stage starts, the more electrons are recorded in the experiment. Thus, the beam charge grows at the PWFA stage.

The energy distribution of BXR quanta generated in the converter under the action of an electron beam with an exponential spectrum is well described by an analytical function of the form [1, 14, 18]

$$\frac{dN_\gamma}{dE} \sim \left(1 - b + \frac{T_e}{E}\right)\exp\left(-\frac{E}{T_e}\right)$$
$$+ \left(b - \frac{E_0}{E} - \frac{T_e}{E}\right)\exp\left(-\frac{E}{T_e}\right), \tag{3}$$

where E_0 is the maximum energy of electrons in the beam; and the constant $b \approx 0.83$. Using the shape of the spectrum (3) and the results of measuring the X-ray yield, the BXR spectrum on the rear side of the Ta converter was reconstructed (Fig. 12). When reconstructing the spectrum, the dependence of the SSDI detector sensitivity η on the quantum energy was taken into account (the detector was only calibrated for $E_\gamma = 1.25$ MeV):

$$\eta(E_\gamma) = \frac{w(E_\gamma)}{w(1.25\ \text{MeV})}\eta(1.25\ \text{MeV}).$$

The coefficients $w(E_\gamma)$ were calculated using the database [19].
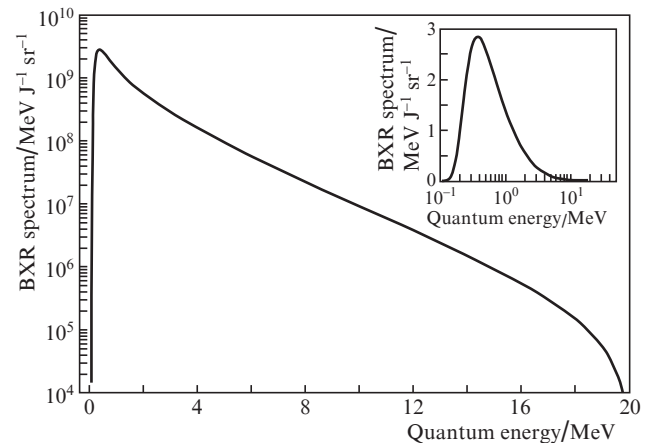
Figure 12. Reconstructed BXR spectrum on the rear side of a 2-mm-thick Ta converter (focusing with a detuning of −800 μm, helium pressure is 60 atm). The inset shows the same spectrum on a linear scale along the ordinate axis.

The average BXR dose generated at a distance of 1 m from the source was 5.4 ± 1.7 mrad per pulse. The conversion of laser radiation energy into BXR energy (according to measurements near the axial direction) is 1.1×10^{-3} sr^{-1}. In conclusion, we note that the SM-LWFA and DLA acceleration regimes at betatron resonance are currently the most promising in terms of generating beams of accelerated electrons of moderate energies (tens of MeV) with a large total charge [20, 21].

5. Conclusions

Experiments on the generation of relativistic electron beams in dense helium jets have been performed using a femtosecond laser. Accelerated electron beams with total charge of

Figure 11. Dependence of the electron beam's total charge Q_{beam} on the coordinate of the abrupt termination point of the plasma channel glow relative to the jet axis X_d (according to images from the side camera) when focusing the laser pulse onto the gas jet edge (− 500 μm). The vertical line shows the position of the gas target axes.

0.2–0.5 nC ($E_e > 4$ MeV), exponential energy spectra with a maximum electron energy of up to 60 MeV and a divergence of up to 300 mrad have been recorded.

It is shown that with an increase in the gas jet density, an increase in the number of accelerated electrons is observed, accompanied by a decrease in the particle energy.

When converting electron beams to BXR, the average radiation dose recorded at a distance of 1 m from the source is 5.4 ± 1.7 mrad per pulse. The transverse size of the emitting region of the tantalum converter is determined from the X-ray image of an object with a large optical thickness and amounted to ~650 μm (FWHM).

It should be noted that the use of a gas target will allow implementation of pulse-periodic regimes of the source operation, which is promising for solving problems of high-spatial-resolution stationary radiography.

References

1. Courtois C., Edwards R., Compant La Fontaine A., et al. *Phys. Plasmas*, **20**, 083114 (2013).
2. Glinec Y., Faure J., Le Dain L., et al. *Phys. Rev. Lett.*, **94**, 025003 (2005).
3. Wang X., Zgadzaj R., Fazel N., et al. *Nat. Commun.*, **4**, 1988 (2013).
4. Leemans W.P., Gonsalves A.J., Mao H.-S., et al. *Phys. Rev. Lett.*, **113**, 245002 (2014).
5. Malka V., Faure J., Marques J.R., et al. *Phys. Plasmas*, **8** (6), 2605 (2001).
6. Mirzaie M., Hafz N., Li S., et al. *Rev. Sci. Instrum.*, **86**, 103502 (2015).
7. Semushin S., Malka V. *Rev. Sci. Instrum.*, **72** (7), 2961 (2001).
8. Sylla F., Veltcheva M., Kahaly S., et al. *Rev. Sci. Instrum.*, **83**, 033507 (2012).
9. Malka V., Coulaud C., Geindre J.P., et al. *Rev. Sci. Instrum.*, **71** (6), 2329 (2000).
10. Masuda S., Miura E., Koyama K., et al. *Rev. Sci. Instrum.*, **79**, 083301 (2008).
11. Buck A., Zeil K., Popp A., et al. *Rev. Sci. Instrum.*, **81**, 033301 (2010).
12. Petrovskii G.T. (Ed.) *Tsvetnoe opticheskoe steklo i osobye stekla. Katalog* (Coloured Optical Glass and Special Glasses. Catalogue) (Moscow: Dom Optiki, 1990) p. 74.
13. https://physics.nist.gov/PhysRefData/Star/Text/ESTAR.html.
14. Galy J., Maucec M., Hamilton D.J., et al. *New J. Phys.*, **9**, 23 (2007).
15. Huntington C.M., Thomas A.G.R., McGuffey C., et al. *Phys. Rev. Lett.*, **106**, 105001 (2011).
16. Masson-Laborde P.E., Mo M.Z., Ali A., et al. *Phys. Plasmas*, **21**, 123113 (2014).
17. O'Shea B.D., Andonian G., Rosenzweig J.B., et al. *Nature Commun.*, **7**, 12763 (2016).
18. Shkolnikov P.L., Kaplan A.E., Pukhov A., et al. *Appl. Phys. Lett.*, **71**, 3471 (1997).
19. http://physics.nist.gov/PhysRefData/Xcom/Text/XCOM.html.
20. Rosmej O.N., Gyrdymov M., Gunther M.M., et al. *Plasma Phys. Control. Fusion*, **62**, 115024 (2020).
21. Shaw J.L., Romo-Gonzalez M.A., Lemos N.. et al. *Nature: Sci. Rep.*, **11**. 7498 (2021).